International Journal of Mechanical Sciences 277 (2024) 109418

Contents lists available at ScienceDirect

International Journal of Mechanical Sciences

journal homepage: www.elsevier.com/locate/ijmecsci

Chip breakage in silk microfibre production using elliptical vibration turning

Zhengjian Wang [a], Xichun Luo [a,*], Jining Sun [b,*], Philipp Seib [c,*], Suttinee Phuagkhaopong [d], Wenkun Xie [a], Wenlong Chang [e], Qi Liu [a], Xiuyuan Chen [a]

[a] Centre for Precision Manufacturing, DMEM, University of Strathclyde, Glasgow G1 1XJ, United Kingdom
[b] School of Mechanical Engineering, Dalian University of Technology, Dalian 116023, China
[c] Pharmaceutical Technology & Biopharmaceutics, Friedrich Schiller University Jena, Jena 07743, Germany
[d] Department of Pharmacology, Chulalongkorn University, Bangkok 10330, Thailand
[e] Innova Nanojet Technologies Ltd., Glasgow G1 1RD, United Kingdom

ARTICLE INFO

Keywords:
Elliptical vibration turning
Smoothed particle hydrodynamics
Chip-breaking mechanism
Silk fibroin
Silk microfibres
Discontinuous chips

ABSTRACT

To overcome the precision limitation and environmental impact of current chemical-based production methods for manufacturing silk microfibres used for targeted drug delivery, this paper presents a high-precision, scalable, eco-friendly mechanical machining approach to produce such microfibres in the form of discontinuous chips obtained through elliptical vibration turning of silk fibroin film using a diamond tool. The length and waist width of fabricated microfibres can be precisely controlled. As each vibration cycle will produce one silk microfibre, complete and deterministic chip breakage becomes an essential and challenging task in this approach due to its unique two-phase structure. Thus, the hybrid FE-SPH numerical simulations and machining experiments were conducted to gain a pioneering and in-depth exploration of the chip-breaking mechanism in this process. It was found that applying a low depth ratio (ratio of the nominal depth of cut to the tool path vertical amplitude) and a high horizontal speed ratio (the nominal cutting speed versus the critical workpiece velocity) could effectively reduce the average tool velocity angle (the angle from the deepest cut to the tool exit point along the cutting direction). A smaller angle would enhance the diamond tool's shearing action and led to the reduction of hydrostatic pressure in the cutting zone and a consequent decrease in the ductility of silk fibroin due to its unique structure dominated by beta-sheet crystallites. The above adjustments collectively facilitated chip breakage. This paper, therefore, established a governing rule for the controlled and repeatable formation of microfibres based on the average tool velocity angle for the first time and revealed that the cutting chips would undergo complete and deterministic breakages once the angle approached below 22.6°. On this basis, the high-precision and scalable manufacturing of silk microfibres with precisely controllable length and waist width was ultimately achieved.

1. Introduction

After several decades of development, targeted drug deliveries based on silk particles have shown great promise in cancer [1] and intra-articular [2] treatments due to silk fibroin's excellent mechanical properties [3], biocompatibility and biodegradability [4]. Drug molecules encapsulated in silk particles can extend their presence in the bloodstream, significantly improving their pharmacokinetics and cell uptake compared to free drugs [5]. Interestingly, the shape factor was discovered to play a critical role in tissue targeting [6]. It is reported that, against silk spheroids [7,8], silk microfibres of tens of microns in length are superior to silk spheroids for drug delivery in terms of targeting and immune clearance [9].

However, current chemical-based processing methods for producing silk particles are facing challenges, including high costs associated with equipment [10,11] and environmental concerns related to chemical usage [12,13]. In contrast, machining techniques offer a high-precision, cost-effective, and chemical-free alternative. Rajkhowa et al. [14] and Kazemimostaghim et al. [15] have demonstrated that the milling process can successfully produce silk spheroids. Yet, these mechanical methods often struggle to maintain shape integrity and size uniformity, and typically suffer from low production rates. Moreover, they are restricted to producing silk spheroids only. Although experimentation

* Corresponding authors.
E-mail addresses: xichun.luo@strath.ac.uk (X. Luo), jining.sun@dlut.edu.cn (J. Sun), philipp.seib@uni-jena.de (P. Seib).

https://doi.org/10.1016/j.ijmecsci.2024.109418
Received 13 March 2024; Received in revised form 23 May 2024; Accepted 23 May 2024
Available online 24 May 2024

Nomenclature

2D	two-dimensional
3D	three-dimensional
FEM	finite element method
FE-SPH	finite element and smoothed particle hydrodynamics
HSR	horizontal speed ratio
SPH	smoothed particle hydrodynamics
α	tool clearance angle, °
θ	tool velocity angle, °
$\theta(t)$	transient tool velocity angle, °
θ_a	average tool velocity angle, °
θ_c	critical value of average tool velocity angle, °
θ_{max}	maximum tool velocity angle, °
π	mathematical constant, 3.1415926
a	tool path horizontal amplitude (cutting direction), μm
b	tool path vertical amplitude (depth of cut direction), μm
D_{ins}	instantaneous cutting diameter, mm
d_c	depth of cut, μm
d_n	nominal depth of cut, μm
f	vibration frequency, Hz
l	fibre length, μm
N	spindle speed, rpm
O	geometric centre of the elliptical tool trajectory
r_d	depth ratio
r_e	tool edge radius, nm
t	time, s
u	upfeed per cycle of the workpiece, μm
V_{cri}	critical workpiece velocity, m/s
V_w	nominal cutting speed, m/s
$\boldsymbol{v}$	transient tool velocity vector, m/s
v_y, $v_y(t)$	y-component of the transient tool velocity vector, m/s
v_z, $v_z(t)$	z-component of the transient tool velocity vector, m/s
w	fibre waist width, μm
y, $y(t)$	tool displacements in the cutting direction, μm
z, $z(t)$	tool displacements in the cutting direction, μm

into the production of silk microfibres through the machining approach is still limited, producing metallic microfibres using vibration-based cutting techniques is well-established. A notable example includes recent work by Li et al. [16], who successfully fabricated short copper microfibres with high length/diameter ratios using vibration chiseling. This method has shown excellent reproducibility and control over the microfibre dimensions, suggesting its potential applicability to silk microfibre production.

Inspired by these advancements, this paper aims to develop a mechanical manufacturing process using elliptical vibration diamond turning for the high-precision and high-efficiency fabrication of silk microfibres as discontinuous chips. This approach is chosen for its superior precision in chip breakage control compared to traditional methods, such as using chip breakers [17] or coolants [18,19]. In the proposed manufacturing process, the silk microfibres are scooped out from silk fibroin film via the elliptical movement of the diamond tool, with each vibration cycle tailored to produce a single silk microfibre.

Silk fibroin, however, presents unique challenges as a natural protein material with properties that differ significantly from ductile metallic materials. Its structural composition, featuring a random amorphous matrix intertwined with beta-sheet crystallites [20], endows silk fibroin with exceptional mechanical and biological properties. In turn, these structural elements critically influence its chip-breaking behaviour under elliptical vibration diamond turning, a phenomenon that remains underexplored. Additionally, the inherent softness and flexibility of silk fibroin [21] mean it may not break cleanly; instead, it is prone to stretching, bending, or tearing, which complicates the production of precisely controlled chips. Furthermore, Wang et al. [22] indicated that material removal during conventional diamond turning of silk fibroin occurs within the ductile regime, further complicating the complete and deterministic breakage of silk cutting chips [17,23].

In summary, there are two primary challenges in developing this manufacturing approach. First, it needs to establish a governing rule that involves careful selection of vibration and machining parameters to achieve complete and deterministic breakage of silk cutting chips, thereby yielding discrete microfibres with high precision in both length and width. Second, the impacts of key processing parameters on the chip-breaking mechanism in this manufacturing process remain poorly understood, presenting a significant knowledge gap which will be thoroughly studied in this paper.

The effects of vibration and machining parameters on chip breakage have been researched for several decades. As previously referred, Li et al. [16] produced copper microfibres using vibration chiseling. Their research identified that the key parameters controlling the geometries of the fabricated microfibres include the tool vibration trajectory, tool shape, backward-moving velocity, and depth of cut. These findings highlight the importance of precise tuning of processing parameters to achieve optimal chip breakage and desired microfibre dimensions. Yang et al. [24] developed an empirical model to predict chip removal during vibration-assisted drilling of Ti-6Al-4V titanium alloys. Their findings suggested that effective chip removal is best achieved with a low rotation speed, a small chip radius, and a high vibration frequency. On this basis, the optimal combination of drilling parameters to maximize processing efficiency for chip removal was provided. Chen et al. [25] established an inequality governing complete chip breakage in ultrasonic vibration drilling of 201 stainless steel, noting that complete chip breakage occurs only when the amplitude/frequency ratio satisfies this inequality. Kim and Choi [26] successfully produced plastic particles in the form of powder-type chips, measuring tens of microns in length, using an ultrasonic vibrator equipped with a single-crystal diamond tool. The tool velocity was set to half the critical cutting velocity; otherwise, long and continuous chips would be produced. Zhao et al. [27] obtained tungsten alloy particles as discontinuous chips using an ultrasonic cutting tool. They found that a smaller phase difference in the vibration could cause the chips to transition from a continuous and smooth shape to a discrete and folded shape. Miyake et al. [28] indicated that it was preferable to apply the vibration in the feed direction with respect to chip breakage when turning 304 stainless steel. They also noted that the effectiveness of vibrations on chip breakage control was tied to the processing parameters used, such as the vibration amplitude relative to the feed rate and cutting speed. These parameters can be transformed into depth ratio and horizontal speed ratio (HSR) through simple mathematical and geometric transformations, whose impacts on chip morphology and chip breakage were also highlighted in Negishi's research [29]. Furthermore, discrete chips with high dimensional consistency were obtained by Negishi using an elliptical vibrator when cutting aluminium with the diamond tool. However, a detailed investigation into how depth ratio and HSR influence the chip-breaking mechanism was lacking, indicating a potential area for deeper research.

Nevertheless, studying the chip-breaking mechanism through solely experimental means is difficult [30], primarily due to the restriction of *in-situ* observation. Simulations serve as a critical supplementary method, offering detailed insights into the chip-breaking process that are difficult to measure in experiments. Hybrid approaches like the FE-SPH formulation have been developed to harness the benefits of both the Finite Element Method (FEM) and Smoothed Particle Hydrodynamics (SPH) [31,32]. Modelling and simulation of micromachining is also one of its significant applications [33]. For example, Takaffoli and

Papini [34] investigated the mechanism of material deformation and removal in the machining of Al6061-T6. Xi et al. [35] studied the chip formation mechanism during the thermally assisted machining of Ti6Al4V alloy with the aid of the hybrid FE-SPH method. This model accurately reproduced the periodic formation of the chip segmentation, where a good agreement with the experimental results regarding cutting force was also achieved. Using a similar hybrid formulation, Zahedi et al. [36] reproduced the orthogonal micro-machining of single-crystal copper and explored its machining mechanics at the micro-scale. Duan et al. [37] conducted the hybrid FE-SPH simulation for the scratching process of monocrystal SiC, which was simplified as a micro-cutting process. Three material removal modes of SiC were illustrated through the simulation results, which closely matched the corresponding experimental outcomes. Recently, Wang et al. [22] explored the formation mechanisms of shear bands and serrated chips in the conventional diamond turning of silk fibroin film using a hybrid FE-SPH formulation. This model accurately replicated chip morphology and specific cutting forces, demonstrating its effectiveness in simulating the chip formation process. Therefore, given its capability to accurately model detailed material behaviour alongside large deformations and fractures during chip formation and breakage, this paper will employ the hybrid FE-SPH formulation to achieve an in-depth exploration of the chip-breaking mechanism involved in this manufacturing process. On this basis, a governing rule for precise control over complete chip breakage will be formulated to guide the high-precision and scalable manufacturing of silk microfibres with customisable sizes.

Building upon the identified challenges and knowledge gaps discussed earlier, this paper is structured as follows. Section 2 introduces the fundamental principles of this processing technique. Subsequently, Section 3 presents a hybrid FE-SPH orthogonal cutting model to reveal the chip-breaking mechanism. Depth ratio and HSR are two critical processing parameters in elliptical vibration diamond turning, both of which significantly influence the average tool velocity angle. On this basis, Section 4 explores the impact of depth ratio and HSR on the chip-breaking performance with the aid of numerical simulations. Section 5 then identifies a critical value for the average tool velocity angle that ensures complete chip breakage, derived from simulation results and experimental trials, to guide the selection of processing parameters. Results from machining trials, as presented in Section 5, demonstrate the effectiveness of the proposed manufacturing approach.

2. Basic principles

This section begins with the detailed preparation process of silk fibroin films from silk solution. Section 2.2 demonstrates the manufacturing principles of silk microfibres using elliptical vibration diamond turning and emphasises the distinctive geometry and consistent uniformity of the produced microfibres. Furthermore, Section 2.3 investigates the significant role of the tool velocity angle in this manufacturing process, highlighting its influence on material removal and chip breakage.

2.1. Material preparation

The silk fibroin solution derived from *Bombyx mori* cocoons must be transformed into silk fibroin films before conducting elliptical vibration diamond turning experiments. The silk cocoons were first boiled in a 25 mM solution of Na_2CO_3 for one hour, followed by dissolving the degummed silk in 9.3 M LiBr at 60 °C for three hours. Afterwards, the solution was dialyzed against water for two days, resulting in a 5 %–6 % w/v concentration of silk fibroin solution. This solution was then diluted with distilled water to a final concentration of 4 % w/v. Next, 5 ml of the silk solution was poured onto an aluminium plate to form silk fibroin films, which were left to dry in the air overnight. This process was repeated three times to increase the thickness. The resulting semi-transparent films contained 15.6 mg of silk fibroin per square centimetre. The samples were kept in a dry, vacuum-sealed environment at a temperature of 25 °C and relative humidity of 60 % to avoid structural alterations before the machining trials.

2.2. Microfibre formation principle

Fig. 1 illustrates the schematic of the manufacturing process to fabricate silk microfibres using elliptical vibration diamond turning.

Fig. 1(a) demonstrates the manufacturing setup where a piece of silk fibroin film (cast on an aluminium plate) was mounted on a vacuum chuck of the ultraprecision diamond turning machine prior to microfibre fabrication. For fabricating silk microfibres, a self-developed elliptical vibrator was employed [38]. As depicted in Fig. 1(b), the elliptical tool vibration led to the formation of silk microfibres in the form of discontinuous chips, which accumulated on the tool rake face. As shown in Fig. 1(c), the microfibres exhibit a unique comma-shaped cross-section characterised by a broader front and a tapering rear. Furthermore, the microfibres' width varies along their length due to the circular cutting edge and elliptical path of the diamond tool, resulting in a design that is more substantial in the middle. Overall, the dimensions of the fabricated silk microfibres are represented by their length l and waist width w, as illustrated in Fig. 1(b). Utilising a high vibration frequency can enhance fibre production rate, as each elliptical vibration cycle will generate one piece of silk microfibre. The fabrication process is further illustrated in Fig. 1(c) from a cross-sectional perspective. The tool trajectory formed by the vibrator is simplified as a series of ellipses, and each of them approximately represents one vibration cycle [29,39]. It is considered as an acceptable approximation when the upfeed of the workpiece in each cycle u is much smaller than the tool path horizontal amplitude a. Hence, the tool's trajectory can be separated into two distinct displacements: one in the cutting direction and the other in the depth-of-cut direction. These displacements are generated by two piezo actuators that are arranged perpendicularly, and their relationships can be described as

$$\begin{cases} y(t) = a\sin(2\pi ft) + V_w t \\ z(t) = b\sin(2\pi ft + \varphi) \end{cases}, \tag{1}$$

where $y(t)$ and $z(t)$ are tool displacements in the y- (cutting) and z- (depth of cut) directions, respectively. a and b are horizontal and vertical tool path amplitudes, respectively. f is the vibration frequency. φ is the phase angle between the tool displacements. V_w is the nominal cutting speed of silk fibroin film that equals $\pi D_{ins} N$. D_{ins} is the instantaneous cutting diameter, and N is the spindle rotation speed.

A parameter, HSR, can be used to characterize the elliptical vibration diamond turning process. It is defined as the ratio of V_w over the critical workpiece velocity V_{cri}:

$$HSR = \frac{V_w}{V_{cri}} = \frac{V_w}{2\pi fa}. \tag{2}$$

It is clear that when V_w is smaller than V_{cri} (i.e. HSR $<$ 1), as demonstrated in Fig. 1(c), the tool trajectories between two successive vibration cycles will overlap. In this case, the diamond tool and the workpiece will contact intermittently; thus, the interrupted cutting can be achieved. Our focus is exclusively on overlapping elliptical vibration diamond turning in this process.

As depicted in Fig. 1(b) and (c), the microfibres' length l is determined by the tool nose radius r_n and depth ratio r_d:

$$l = 2\sqrt{{r_n}^2 - (r_n - br_d)^2}. \tag{3}$$

In Eq. (3), the depth ratio is the ratio of the nominal depth of cut d_n and the tool path vertical amplitude b. The nominal depth of cut is the vertical distance between the silk fibroin surface and the deepest point that the diamond tool can reach. As expressed in Eq. (3), the microfibres' length can be easily tuned by changing the tool nose radius and depth

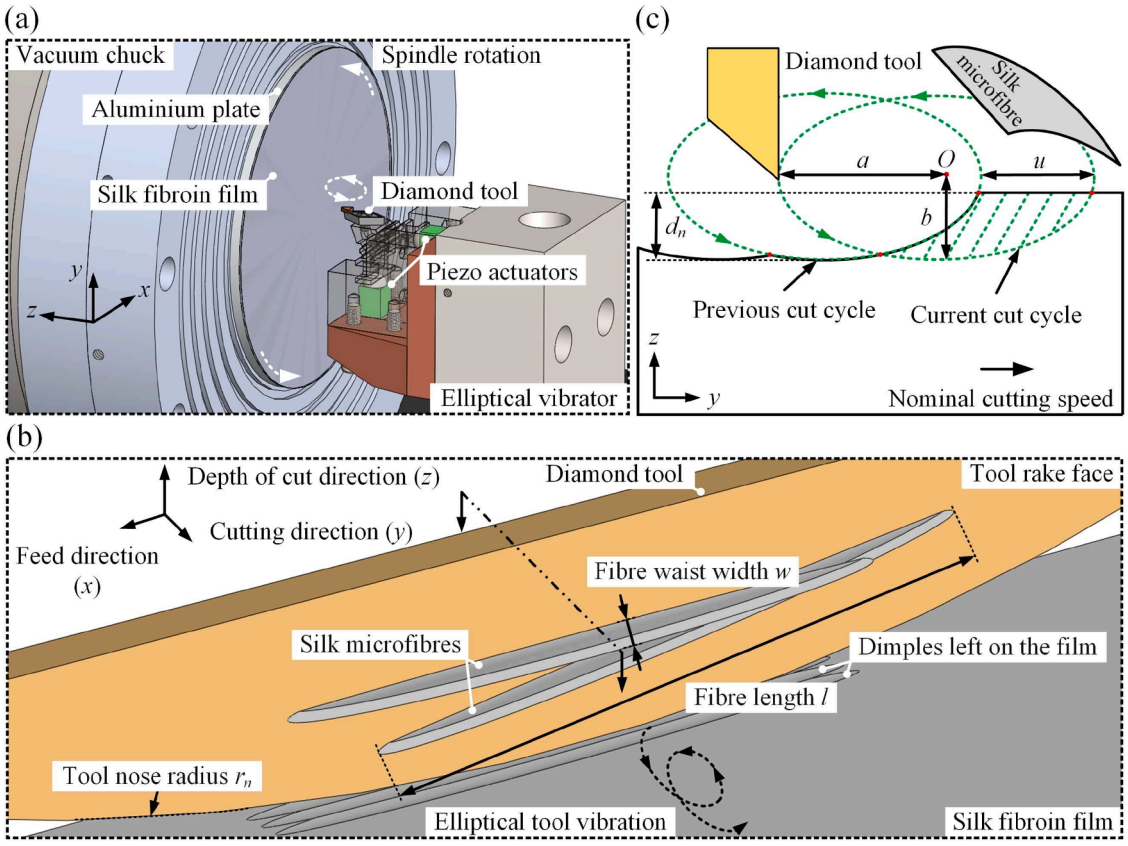

Fig. 1. 3D schematics illustrate the formation principle of silk microfibres with the (a) manufacturing setup and the (b) enlarged view of the manufacturing process. (c) 2D schematic of the manufacturing process from a cross-section view by slicing along the black dashed double-dot line.

ratio. Overall, this method paves the way for the scalable fabrication of silk microfibres with outstanding uniformity in geometry.

2.3. Tool velocity angle in elliptical vibration diamond turning

In conventional diamond turning, the tool velocity angle remains constant throughout the machining process. However, as illustrated in Fig. 2, in elliptical vibration diamond turning process, the tool velocity angle, denoted as θ, varies over time along the trajectory of the tool. The tool velocity angle plays a significant role in the material removal process and can have a substantial impact on the ductile-brittle transition of the work material and even the chip-breaking behaviour, as mentioned in a previous study [40]. Thus, it can be regarded as a dominating parameter to achieve deterministic and complete chip breakage in this process.

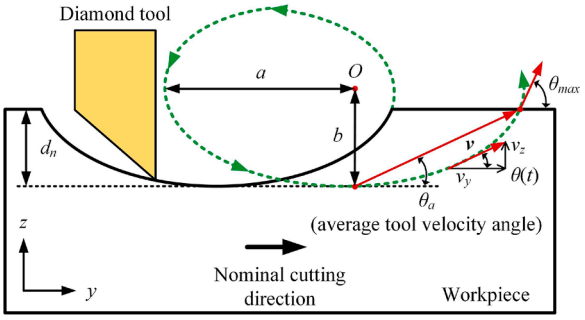

Fig. 2. Schematic illustration of the tool velocity angle in elliptical vibration diamond turning. The green dashed line shows the elliptical trajectory of the diamond tool, and the angles between the red arrows and the nominal cutting direction (positive direction of y-axis) indicate the tool velocity angles in different positions.

The transient tool velocity angle $\theta(t)$ is defined as the angle of the transient tool velocity vector $\boldsymbol{v}$ relative to the y-axis:

$$\theta(t) = \tan^{-1}\left|\frac{v_z(t)}{v_y(t)}\right|, \tag{4}$$

where $v_y(t)$ and $v_z(t)$ are the components of the tool velocity vector on the y- and z-axis, respectively. It is worth noting that for an effective and complete chip breakage, only the processing condition with a nominal depth of cut d_n less than the tool path vertical amplitude, i.e. $r_d < 1$, is considered. To simplify the analysis, a neutral rake angle tool is employed.

As shown in Fig. 2, θ_{max} is the maximum tool velocity angle, which is the transient velocity angle when the tool/workpiece engagement is ended. The average tool velocity angle, denoted as θ_a, is the angle between the nominal cutting direction and the connection line linking the deepest point (point A) that the tool can reach and the point where the tool ends the engagement with the workpiece (point B). The trajectories of two consecutive vibration cycles can be simplified as identical ellipses when HSR is small. In this case, θ_a can be derived as

$$\begin{cases} \theta_a = \tan^{-1}\left(\dfrac{b}{a'}\dfrac{r_d}{\sqrt{1-(1-r_d)^2}}\right), \\ a' = a(1+\pi HSR) \end{cases} \tag{5}$$

where a' is the actual tool path horizontal amplitude in elliptical vibration diamond turning. Based on Eq. (5), a higher HSR results in the enlargement of the tool path horizontal amplitude as the tool trajectory becomes horizontally stretched in this direction. The depth ratio and HSR play a significant role in influencing the average tool velocity angle

and consequently affect the chip-breaking process greatly. Notably, a small depth ratio and a high HSR can reduce the average tool velocity angle. It is worth mentioning that Eq. (5) is valid when the value of HSR remains sufficiently low.

Nevertheless, as HSR increases, the impacts of depth ratio and HSR on the average tool velocity angle exhibit a similar trend. This is because, as illustrated in Fig. 2, the toolpath between points *A* and *B* is consistently concave. The upcoming sections will establish a microfibre formation law based on the average tool velocity angle for a complete chip breakage, which enhances the high-precision and scalable production of silk microfibres.

3. Hybrid FE-SPH modelling

This section introduces the development of a hybrid FE-SPH numerical model to analyse the chip-breaking mechanism in elliptical vibration diamond turning of silk fibroin. Section 3.1 details the setup of this model and describes the simulation conditions that reproduce the elliptical tool trajectories. Furthermore, the model evaluation and verification through simulations and experimental comparisons are demonstrated in Section 3.2 to showcase the model's effectiveness in accurately predicting chip morphology and specific cutting force.

3.1. Orthogonal cutting model

As mentioned before, a complete chip breakage is essential for this manufacturing process, so its chip-breaking mechanism must be investigated prior to production. The traditional finite element method requires considerable effort to establish accurate criteria for chip/workpiece separation and to manage extreme grid distortions [41–43]; therefore, a hybrid FE-SPH numerical model for this process is developed owing to its inherent ability to capture the natural flow of machined materials. In this paper, elliptical vibration diamond turning is treated as an orthogonal cutting process, making it easier to analyse and understand [44,45]. This simplification also significantly decreases the computational power requirement [46]. In this study, thermal effects are considered negligible and not explicitly modelled for several reasons [47]. Firstly, the periodic separation allows the tool and workpiece to cool down between operations [48,49], effectively dissipating accumulated heat and minimizing thermal build-up in the silk fibroin film, which helps maintain consistent material properties and dimensional stability. Additionally, the use of submicron depths of cut and low material removal rates significantly minimize thermal effects during the machining process [50]. Moreover, the cutting experiments were carried out at low cutting speeds to further reduce heat generation and its impact on the material.

A 3D model of a silk fibroin workpiece, measuring 15 μm × 15 μm × 0.5 μm, was created within an orthogonal cutting framework using LS-PrePost. Fig. 3 shows the hybrid FE-SPH numerical model established in this work.

The workpiece was divided into two distinct domains: one represented the Smoothed Particle Hydrodynamics (SPH) domain with dimensions of 9.5 μm × 7 μm × 0.5 μm, implemented using the renormalised formulation, while the remaining portion represented the Finite Element (FE) domain. The FE region was discretised using eight-node Lagrangian solid elements. For the SPH domain, a particle density of 0.1 μm was chosen, ensuring an adequate number of SPH particles across the thickness of the chip. Therefore, the total number of SPH particles reached approximately 40,896. The mesh size for the FE domain was set to 0.25 μm. Additionally, two symmetry planes were enforced on the front and back faces of the SPH domain.

Moreover, fixed boundary conditions were applied to the bottom and left-hand faces of the workpiece. At the interface between the FE and SPH domains, a tied contact formulation was employed to couple the Lagrangian meshes and SPH particles, as its effectiveness had been verified in previous research [36]. The tool rake angle was set to 0°,

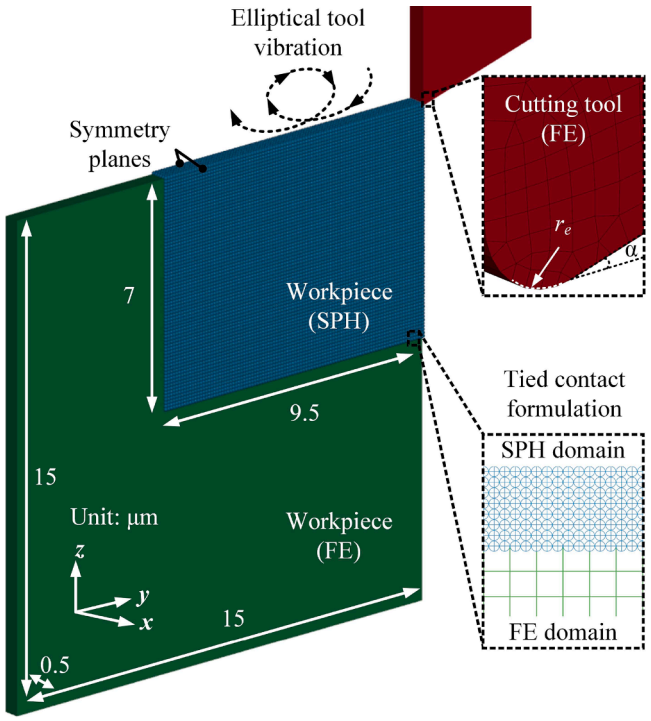

Fig. 3. Illustration of hybrid FE-SPH numerical model for elliptical vibration diamond turning. This figure depicts a two-domain workpiece, the green FE domain and the blue SPH domain, coupled via a tied contact formulation. The cutting tool is modelled in FE, and the red dashed line indicates its elliptical vibration trajectory. Dimensions are given in micrometres (μm).

while the clearance angle α was 15°. The cutting edge radius r_e of the diamond tool, specified as 60 nm in the hybrid model according to technical data from the tool manufacturer, was explicitly and naturally incorporated into the simulation to account for its impact on stress and strain distribution within the machining area. Additionally, the mesh around the tool tip was adequately refined to improve the modelling accuracy. The diamond cutting tool has a density of 3.5 g/cm^3 and a Young's modulus of 1050 GPa, while its Poisson's ratio is 0.1. The coefficient of Coulomb friction between the tool and workpiece was determined as 0.12 [51].

The Cowper-Symonds material model, as utilised in the authors' previous work [22], was employed to characterize the damage behaviour of the silk fibroin during elliptical vibration diamond turning. The specific material parameters for silk fibroin are presented in Table 1.

The diamond tool in the numerical model oscillates periodically in the cutting and depth of cut directions to reproduce the elliptical tool trajectories in elliptical vibration diamond turning. The phase angle between the two directions was 90°. The tool displacements in the *y*- (cutting) and *z*- (depth of cut) directions are given in the following equations:

$$\begin{cases} y(t) = a\cos(2\pi ft) - V_w t - a \\ z(t) = -b\sin(2\pi ft) \end{cases}, \tag{6}$$

Table 1
Material parameters for silk fibroin [52–54].

Material parameters	Silk fibroin
Density (g/cm^3)	1.4
Young's modulus (GPa)	5.2
Poisson's ratio	0.3
Static yield stress (MPa)	70
Tangent modulus (MPa)	172.4
Cowper-Symonds parameter *p*	7
Cowper-Symonds parameter *D* (s^{-1})	1140

where a and b are the tool path amplitudes in corresponding directions. f is the vibration frequency. V_w is the nominal cutting speed of the workpiece.

The key distinction between conventional and elliptical vibration diamond turning processes lies in the nature of tool/workpiece contact. In the conventional process, the tool maintains permanent contact with the workpiece. Conversely, in the elliptical vibration process, the tool-workpiece contact becomes intermittent.

3.2. Model evaluation and verification

In order to evaluate and verify the orthogonal cutting model established in this paper, a series of simulations were conducted for conventional diamond turning of silk fibroin with a cutting speed of 1.35 m/s and different depths of cut. The comparison between the simulated chip morphology and the experimental results from the authors' previous work [22] is illustrated in Fig. 4.

Both simulated chips exhibited visible chip segmentation and shear localization on the free surface, aligning with the corresponding measurement results in Fig. 4(b) and (d). The simulated shear band spacing, denoted as S, showed good agreement with the experimental values for different depths of cut. Specifically, simulations with a depth of cut of 1.5 μm yielded an approximate shear band spacing of 1.8 μm, while simulations with a depth of cut of 2 μm resulted in a simulated shear band spacing of approximately 2.3 μm. Notably, the formation mechanism of serrated chips was linked to the hierarchical structure of silk fibroin. As a result of the high shearing action in ultraprecision diamond turning, the increased number of ruptured H-bonds made the beta-strand interfaces act as slip planes. This led to interstrand slip motions that accumulated and formed shear bands, ultimately leading to the formation of serrated chips. These findings were consistent with what had been previously reported by the authors [22]. Overall, the high consistency between the simulations and the measured values demonstrates the accuracy of the hybrid model established in this paper.

In addition, a good estimation of the specific cutting force was also achieved with the aid of this model. Fig. 4(e) compares the simulated and experimental specific cutting forces. When the depth of cut was set to 2 μm, the specific cutting force attained a value of 300.2 μN/μm^2, representing 56.7 % of the value measured in experiments. Additionally, at a depth of cut of 1.5 μm, the specific cutting force derived from numerical simulations was 314.8 μN/μm^2, equating to 49.2 % of the experimental outcome. The estimation error arose from the omission of strain and thermal effects in Cowper-Symonds material model, which only accounts for strain-rate hardening. However, the reliable prediction of specific cutting force and chip morphology validated the effectiveness of the established hybrid FE-SPH model.

4. Parametric study on chip-breaking mechanism

This section presents the parametric study conducted with the hybrid FE-SPH numerical model, as established in the previous section, to explore how the average tool velocity angle impacts chip-breaking behaviour. The effect of HSR and depth ratio on chip breakage were analysed in Sections 4.1 and 4.2, respectively. Both parameters significantly influence the average tool velocity angle, and the effect of this angle on the chip-breaking mechanism is revealed at the end of this section.

4.1. Effect of HSR

Previous studies have highlighted the significant influence of the tool velocity angle on hydrostatic pressure and shear stress in elliptical vibration diamond turning [40,55]. Understanding their distribution can provide insights into chip-breaking behaviours. Therefore, to investigate the effect of HSR, Fig. 5 illustrates the distribution of hydrostatic pressure and von Mises stress under different values of HSR at two critical moments: when the tool/workpiece engagement ended and when the tool withdrew from the chip (or at the moment of chip breakage if it occurred before tool withdrew). These two moments were chosen for analysis as they are key transition points for observing how pressure and stress concentrations dissipate or transform. A vibration frequency of 20

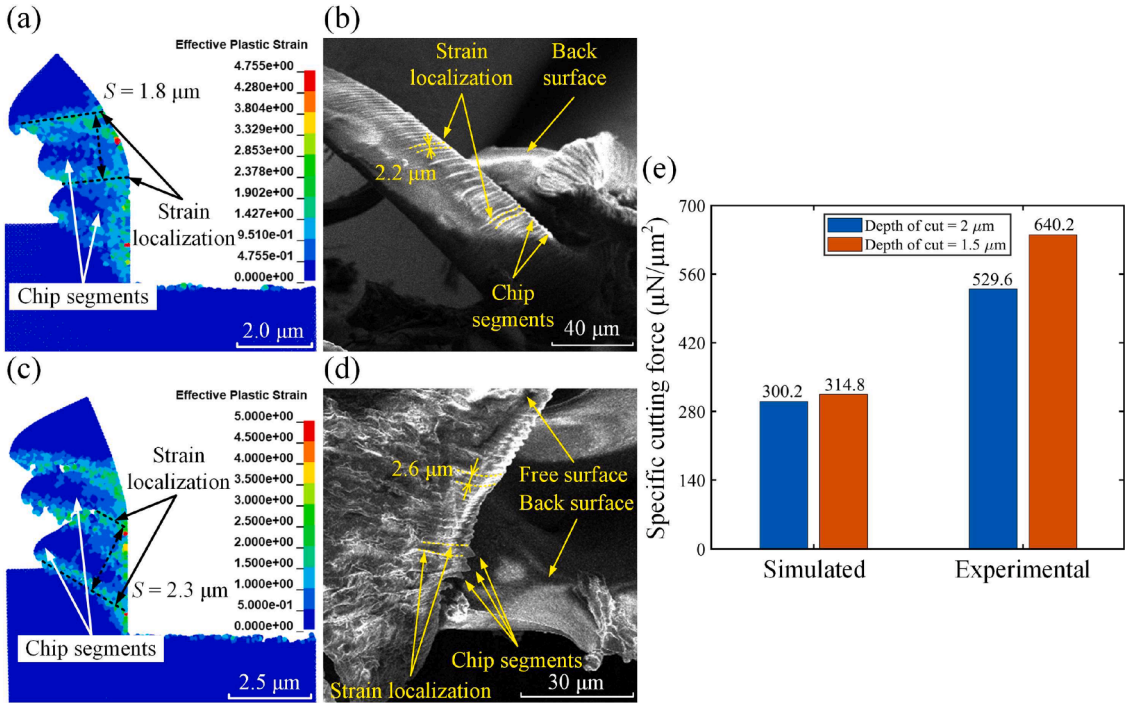

Fig. 4. Comparison between the (a) simulated chip morphology with a depth of cut of 1.5 μm and (b) experimental chip morphology at the same depth of cut. Comparison between the (c) simulated chip morphology with a depth of cut of 2 μm and (d) experimental chip morphology at the same depth of cut. (e) Comparisons between simulated results and experimental findings of the specific cutting force with depth of cut of 1.5 μm and 2 μm.

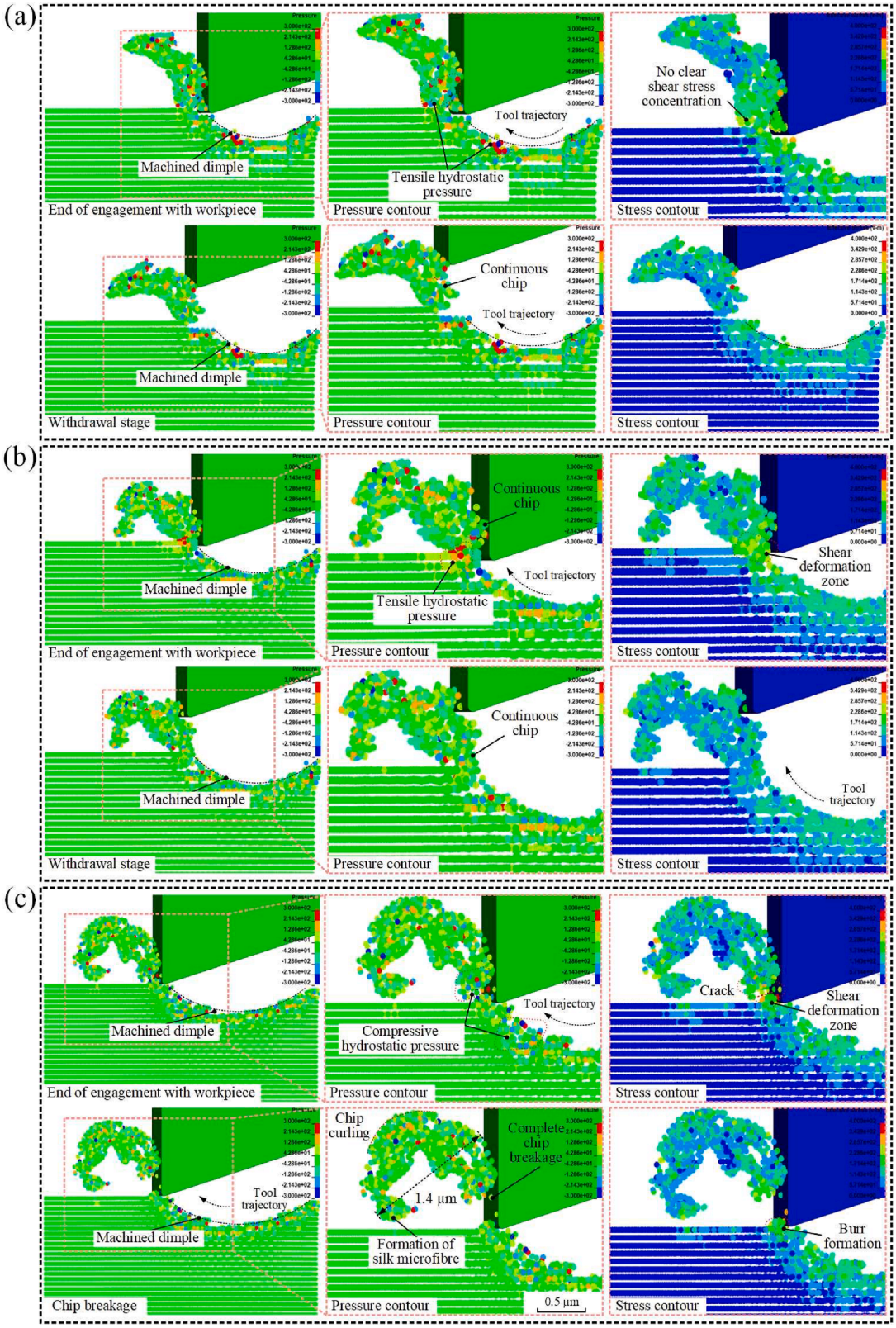

Fig. 5. Distribution of hydrostatic pressure (unit: MPa) and von Mises stress (unit: MPa) in elliptical vibration diamond turning with (a) HSR = 0.1 ($\theta_a = 27.3°$), (b) HSR = 0.3 ($\theta_a = 23.0°$) and (c) HSR = 0.9 ($\theta_a = 15.5°$). This figure illustrates the evolution of hydrostatic pressure and von Mises stress and their impacts on the transformation of chip morphology. Across all panels, the distribution of pressure and stress within the workpiece is represented by consistent colour scales, respectively. The pink dashed frame encloses the enlarged view of interest, highlighting the details of pressure and stress evolution. The tool trajectories are demonstrated in black dashed arrows. The red dashed line shows the crack in the chip, while the red dotted line encircles the concentration area of hydrostatic pressure and the shear stress deformation zone.

kHz was selected for all simulation cases, considering the constriction of available computational power. At the same time, the tool path amplitudes a and b were set to 1 μm and remained constant. A fixed depth ratio of 0.5 was employed in all cases, indicating a nominal depth of cut of 0.5 μm. The same colour legend scale was utilised in each figure to monitor the pressure and stress variations. This allows for consistent comparison and analysis of pressure and stress changes across different scenarios.

As depicted in Fig. 5, the HSR was increased from 0.1 to 0.9, leading to a gradual reduction in the average tool velocity angle from 27.3° to 15.5°. It is worth mentioning that the machined dimples with a curved shape were consistently visible across all figure panels, accurately replicating the elliptical tool trajectories. Additionally, the formation of these dimples aligned well with the schematic of the manufacturing process illustrated in Fig. 1(c). When the HSR was 0.1, tensile hydrostatic pressure could be initially observed in the region ahead of the tool rake face and below the tool edge. As the HSR increased, the hydrostatic pressure diminished and transitioned to high compressive hydrostatic pressure. Normally, high compressive hydrostatic pressure is known to enhance ductility [56–59]. But, in the case of silk fibroin, the scenario was exactly the opposite due to its unique structures. Fig. 6 demonstrates the structure of silk fibroin and its pressure-dependent structural transition.

Silk fibroin is a protein material that consists of two primary phases; the random amorphous matrix and beta-sheet crystallite. Increased hydrostatic pressure (typically above 100 MPa) can lead to a higher degree of crystallinity by promoting the formation of more ordered beta-sheet structures that are responsible for the material's strength and structural rigidity [60]. Yet, as illustrated in Fig. 5(c), local pressure could reach over 200 MPa, causing an excessive increase in the beta-sheet content. The silk fibroin became over-rigid, potentially decreasing the ductility of silk fibroin. Also, an inherent trade-off between strength and ductility means that a higher strength comes at the expense of ductility [61,62]. In short, the ductility of the silk fibroin was decreased because of high compressive hydrostatic pressure, contributing to crack initiation and thus chip breakage in the manufacturing process [63–66]. When the HSR reached 0.9, a complete chip breakage was achieved, and a discontinuous chip was formed, as illustrated in Fig. 5(c). This chip exhibited a thinner front and a thicker back, aligning with the anticipated chip geometry as displayed in Fig. 1(c), despite a slight chip curling due to the bending moment and plastic deformation formed at the cutting zone [67–70]. The accurate prediction of chip geometry was attributed to the SPH technique's ability to reproduce the natural material flow [71–73], which validates the accuracy of the established model in turn. Fig. 5(c) demonstrates that, under an HSR of 0.9 and a depth ratio of 0.5, the predicted waist width w of the fabricated silk microfibres was about 1.4 μm.

Regarding von Mises stress, Fig. 5(a) illustrates that there was no apparent shear stress concentration in front of the tool's rake face when the HSR was set at 0.1. However, as the HSR increased, there was a gradual accumulation and concentration of shear stress, leading to the formation of a shear deformation zone within the chip. This phenomenon arose due to the smaller tool velocity angle associated with higher HSR values, enhancing the extrusions and shearing actions of the diamond tool. As shown in Fig. 5(c), with the advance of the diamond tool and shear strain accumulation, a crack in the chip was initiated and propagated along the narrow shear deformation zone. Ultimately, the complete chip breakage was achieved.

4.2. Effect of depth ratio

Fig. 7 displays the distribution of hydrostatic pressure and von Mises stress under various depth ratios. In the manufacturing operation, two significant moments were observed: when the tool disengaged from the workpiece and when the tool withdrew from the chip (same choices as in Fig. 5). Meanwhile, the HSR remained constant at 0.4 for all cases. A consistent colour legend with the same scale was utilised in both figures. This allows for a direct comparison of pressure and stress changes.

Fig. 7 shows the impact of reducing the depth ratio on the chip-breaking dynamics of silk fibroin. When the depth ratio was decreased from 0.7 to 0.4, there was a notable reduction in the average tool velocity angle, from 25.6° to 18.9°. This change coincided with a shift in hydrostatic pressure in front of the tool's rake face from nearly neutral to highly negative, as depicted in Fig. 7(a) and (b). This transition indicates a significant increase in compressive hydrostatic pressure, which is known to reduce the ductility of silk fibroin, as previously discussed. Additionally, the materials with lower ductility are more likely to reduce or eliminate burr formation during machining [74–76]. This relationship was evidenced by the results presented in Fig. 7(b) and (c), where a significantly smaller burr was observed at a depth ratio of 0.4 compared to those at a depth ratio of 0.5. The decrease in ductility, coupled with the diamond tool's enhanced shearing action (enabled by a lower average tool velocity angle), plays a crucial role in effectively suppressing burr formation. This is further supported by the stress contour illustrated in Fig. 7(a), which highlights the formation of a localized shear stress area at a depth ratio of 0.7. As the depth ratio decreased, the shear stress and strain accumulated, forming a shear deformation zone. The formation of silk microfibres was directly attributed to these phenomena. As Fig. 7(b) demonstrates, the reduction in depth ratio to 0.5 or below facilitated the initiation and propagation of cracks within the silk fibroin chip. This process led to complete chip breakage, ultimately resulting in the formation of loose and discrete silk microfibres.

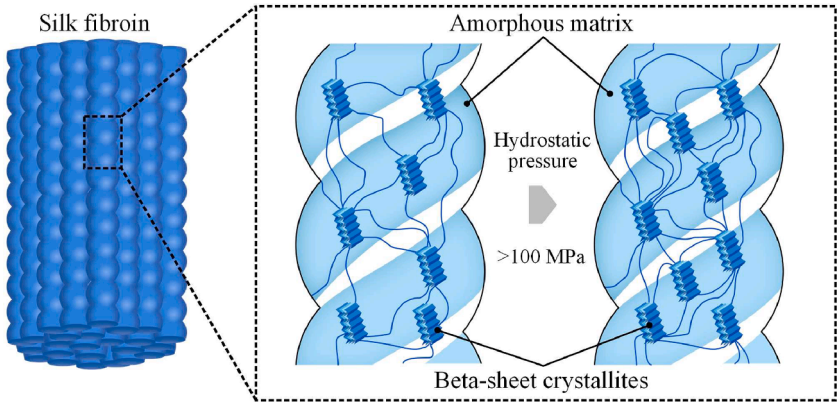

Fig. 6. Schematic illustration of the two-phase structure of silk fibroin and its hydrostatic pressure-induced transition. The image on the left illustrates the initial array of fibroin fibres. The central and right images offer magnified views of the structure, showing the transformation of beta-sheet crystallites when subjected to hydrostatic pressures over 100 MPa.

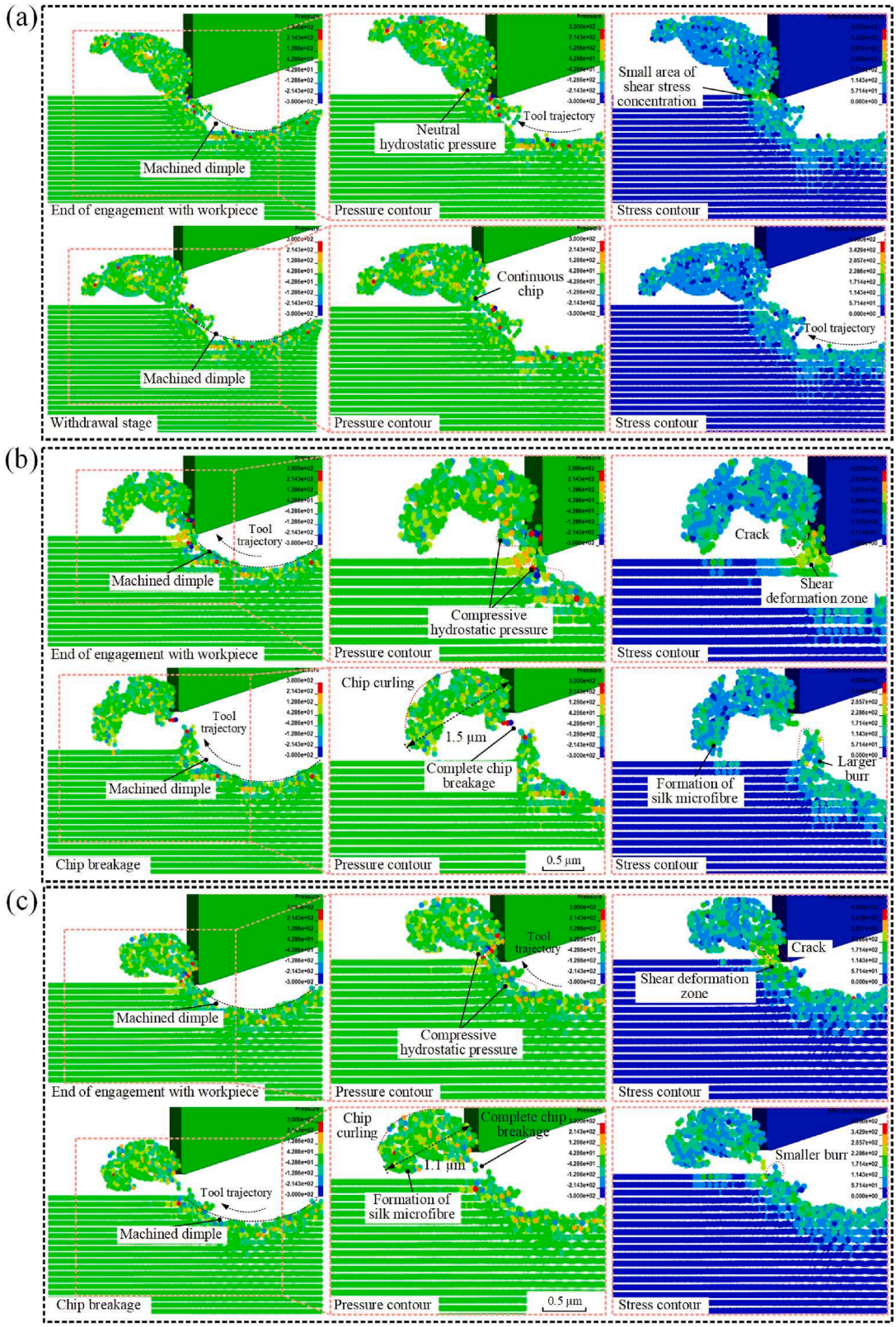

Fig. 7. Distribution of hydrostatic pressure (unit: MPa) and von Mises stress (unit: MPa) in elliptical vibration diamond turning with (a) $r_d = 0.7$ ($\theta_a = 25.6°$), (b) $r_d = 0.5$ ($\theta_a = 21.3°$) and (c) $r_d = 0.4$ ($\theta_a = 18.9°$). This figure depicts the progression of hydrostatic pressure and the corresponding transformation in chip morphology. Across all panels, the pressure and stress distribution within the workpiece are represented by the same colour scale, respectively. The pink dashed frame encloses the enlarged view of interest, highlighting the details of pressure and stress evolution. The tool trajectories are demonstrated in black dashed arrows. The red dashed line shows the crack in the chip, while the red dotted line encircles the concentration area of hydrostatic pressure and the shear stress deformation zone.

In conclusion, the study demonstrates that a reduction in the average tool velocity angle facilitates complete and precise chip breakage in elliptical vibration diamond turning of silk fibroin. This achievement is attributed to the combined effects of weakened ductility of the silk fibroin and enhanced shearing action of the diamond tool. Eventually, the rule governing the controlled formation of silk microfibres, based on the critical value of the average tool velocity angle, is established. According to the simulation results, the critical value was initially confirmed within the range from 21.3° to 23.0°. However, further experimental investigations are necessary to determine its specific value, which will be discussed in Section 5.

5. Manufacturing trials to fabricate silk microfibres

In this section, a series of manufacturing trials were conducted on an ultraprecision diamond turning machine equipped with an elliptical vibrator to determine the threshold value of the average tool velocity angle for producing silk microfibres. The details of the manufacturing setup and experimental conditions are elaborated in Section 5.1, while the outcomes and analyses of these experiments are presented in Section 5.2.

5.1. Manufacturing setup and conditions

Fig. 8 illustrates the setup employed for the manufacturing process. A round nose tool with a nose radius of 0.5 mm, a rake angle of 0°, and a clearance angle of 15° was utilised for the cutting operation. A three-component dynamometer (9129AA, Kistler) was mounted beneath the tool holder to measure the cutting forces. Furthermore, a scanning electron microscope (S3700-N, Hitachi) was employed to observe and analyse the silk microfibres.

As illustrated in Fig. 8, a high-performance function generator (TGF4042, Aim-TTi) and a power amplifier (E01.A2, CoreMorrow) were employed to generate sinusoidal signals accurately. These signals are crucial for maintaining the correct frequencies and phase relationships, which are essential for coordinating the orthogonal movements of the diamond tool along the *y*- and *z*-axes. The mechanical stability of the manufacturing system is ensured through the use of a pair of rigid piezoelectric actuators (PSt150, Piezomechanik) and a well-developed elliptical vibrator. The efficacy of this configuration has been demonstrated in the authors' previous work [38], where the machining accuracy of the vibrator was validated by producing micro-dimple arrays and two-tier microstructured surfaces with machining errors below 11 %, demonstrating that this configuration can effectively mitigate asynchronous motion between the *y*- and *z*-axes. Additionally, prior to operational use, the system underwent rigorous calibration to confirm that the actuators respond accurately to the control signals. The processing parameters for four sets of manufacturing trials, designated as I, II, III and IV, are presented in Table 2. The experiment involved the application of two vibration frequencies: 100 Hz and 500 Hz. The horizontal and vertical amplitudes of the tool path were approximately 0.75 μm and 1 μm, respectively. The depth ratio in sets I and II was 0.5. However, a depth ratio of 0.7 was specifically chosen for set III. A uniform feed rate of 150 μm/rev was used throughout the experiments to maintain the cutting in a non-overlapping scheme.

5.2. Results and discussions

As displayed in Fig. 9, the measured cutting forces are compared between the elliptical vibration diamond turning experiment (set I) and its conventional counterpart (set II), both conducted at the same nominal cutting speed of 0.42 mm/s. Notably, the measured cutting forces in set I were collected under an HSR of 0.9.

Fig. 9 demonstrates that the peak cutting force in the elliptical vibration diamond turning is slightly higher than that in conventional diamond turning. The overshoot of the cutting force is attributed to the vibration impact of the diamond tool. Nevertheless, the valley values of cutting force reach nearly zero in each vibration cycle, indicating a complete tool/workpiece separation. The noise in the force data during the acquisition process resulted in the inability to obtain an absolute zero value. The average cutting force in vibration cutting is significantly

Table 2
Processing parameters for manufacturing trials.

Set	Cutting mode	Vibration frequency (Hz)	HSR	Nominal depth of cut (μm)
I	Elliptical vibration	100	0.1; 0.3; 0.5; 0.7; 0.9	0.5
II	Conventional	N/A	N/A	0.5
III	Elliptical vibration	100	0.3; 0.9	0.7
IV	Elliptical vibration	500	0.9	0.5

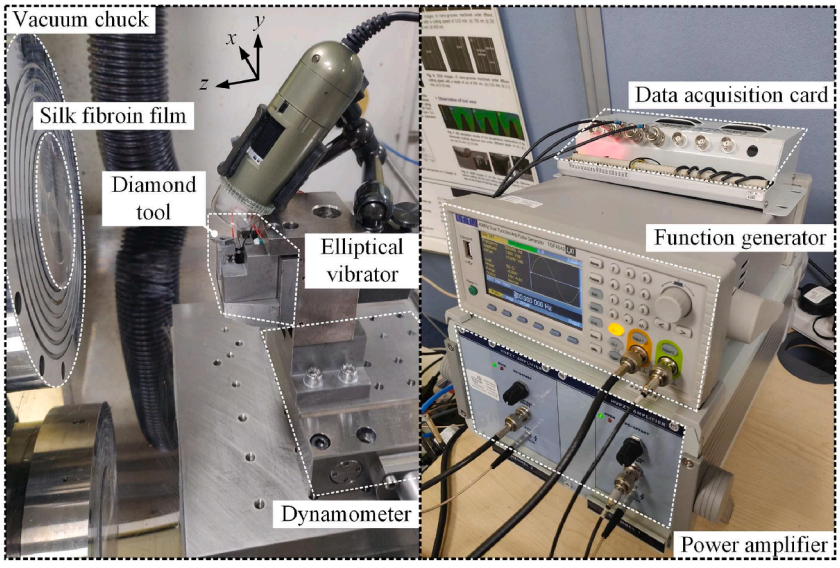

Fig. 8. Experimental setup for manufacturing silk microfibres using elliptical vibration diamond turning. The left panel of this figure illustrates the manufacturing configuration, while the right one depicts the configuration for signal generation and data acquisition.

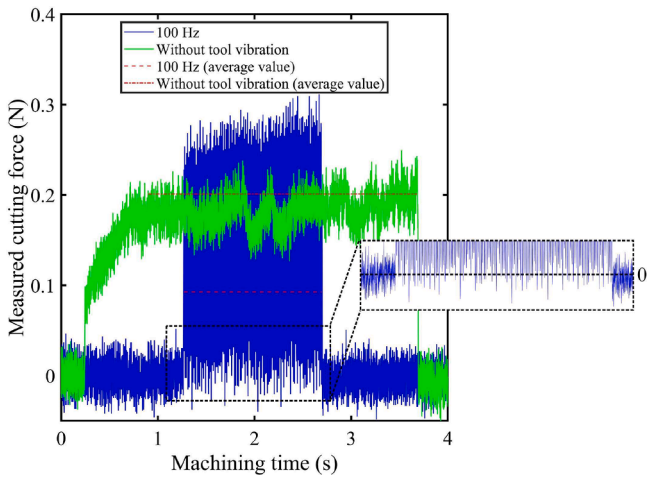

Fig. 9. Comparison between conventional diamond turning (d_c = 0.5 μm) and elliptical vibration diamond turning (f = 100 Hz; HSR = 0.9; r_d = 0.5) on cutting force variations. The enlarged view (enclosed by red dashed lines) illustrates the minimum value of the cutting force measured in elliptical vibration diamond turning.

reduced by 53.9 % compared to conventional diamond turning, which also results from the intermittent tool/workpiece contact after applying the elliptical vibration [77,78]. The proposed hybrid model has effectively reproduced the cyclical fluctuations of the cutting force in this process. Given that the actual depth of cut varies along the tool path, the unit cutting force was chosen as an indicator for normalization purposes. Fig. 10 illustrates the oscillation of the unit cutting force and the contour of the effective plastic strain from the initiation of tool/workpiece contact to their disengagement.

The HSR and depth ratio adopted in the simulation are the same as those shown in Fig. 9, with the only difference being the vibration frequency set at 20 kHz. This frequency was chosen to significantly reduce the computational demands due to limited access to computing power. The simulation duration is constrained to 20 μs for the same reason; nevertheless, it covers an entire cutting cycle. Within each cutting cycle, as depicted in Fig. 10, the unit cutting force increases continuously until the diamond tool reaches the deepest point of the tool path, after which it gradually decreases to zero. Stress accumulates as the cutting tool advances, leading to the formation of cracks on the cutting chip once it exceeds the strength of silk fibroin. As a result, the stress gets released, as indicated by a slight decline in the unit cutting force. As the cutting force surpasses its peak value, the drop in force caused by crack formation becomes more pronounced due to the decreasing amount of removed material. This phenomenon persists throughout the cutting process until complete chip breakage occurs.

Figs. 11, 13 and 14 display the chip morphologies obtained in the experiments of sets I, III and IV, respectively. The caption of each figure provides the average tool velocity angles corresponding to specific processing parameters.

As illustrated in Fig. 11(b), the vibration marks were clearly identifiable on the continuous chips, and their formation was successfully reproduced using the established hybrid numerical model. Fig. 12 illustrates the comparison of chip morphology between the experimental continuous chip and its simulated counterpart.

As shown in Fig. 12(a), the chip's back surface displayed a periodic smooth wavy pattern because of the cutting action produced by the diamond tool's elliptical motion trajectory. The dashed yellow lines delineate the boundary between two adjacent cuts. The wavelength of the wavy pattern of the chip from the SEM image was about 1.5 μm, while the simulated wavelength was 1.3 μm, validating the hybrid model's accuracy in replicating the actual manufacturing process.

In the experiments carried out in set I, with the increase in, there was a progressive decline in the average tool velocity angle, from 34.5° to 20.3°. During this process, the chip structure evolved from being continuous to semi-continuous. When the average tool velocity angle approached 22.6°, the discrete silk microfibres began to form (instead of the formation of ribbon-shaped chips), indicating a complete and stable chip breakage. The transformation of chip morphology from continuous to discontinuous is consistent with the simulation results presented in Section 4. Also, the fabricated microfibres exhibit a thicker design in the middle, agreeing well with the anticipated fibre geometry depicted in Fig. 1(c). Based on the chip morphology depicted in Fig. 11, it was determined that the critical value of the average tool velocity angle necessary for complete chip breakage was between 22.6° and 25.6°. Simultaneously, as noted in Section 4, the simulated threshold for chip breakage ranged from 21.3° to 23.0°. Two ranges overlapped slightly (22.6° to 23.0°), indicating consistency between simulated and experimental findings. Considering both the simulation and experimental results, the critical value was identified as 22.6°. Maintaining the average tool velocity angle below this threshold is essential to fabricate silk microfibres. Furthermore, the smaller the average tool velocity angle,

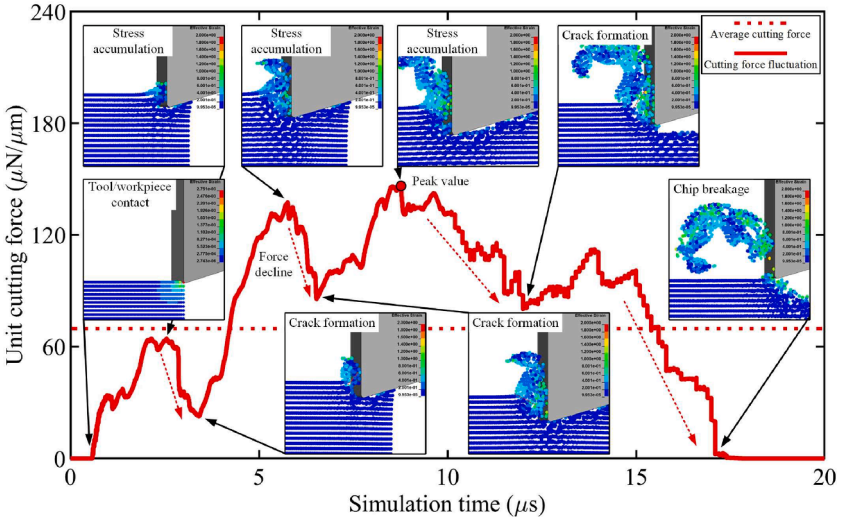

Fig. 10. The simulated unit cutting force (unit: μN/μm) oscillation from the moment the diamond tool contacts with the workpiece until their separation and the contour of the effective plastic strain at the corresponding moment (f = 20 kHz; HSR = 0.9; r_d = 0.5). The solid red line shows the cutting force oscillations, while the red dashed line shows its average value. The cracks are depicted in red dotted lines.

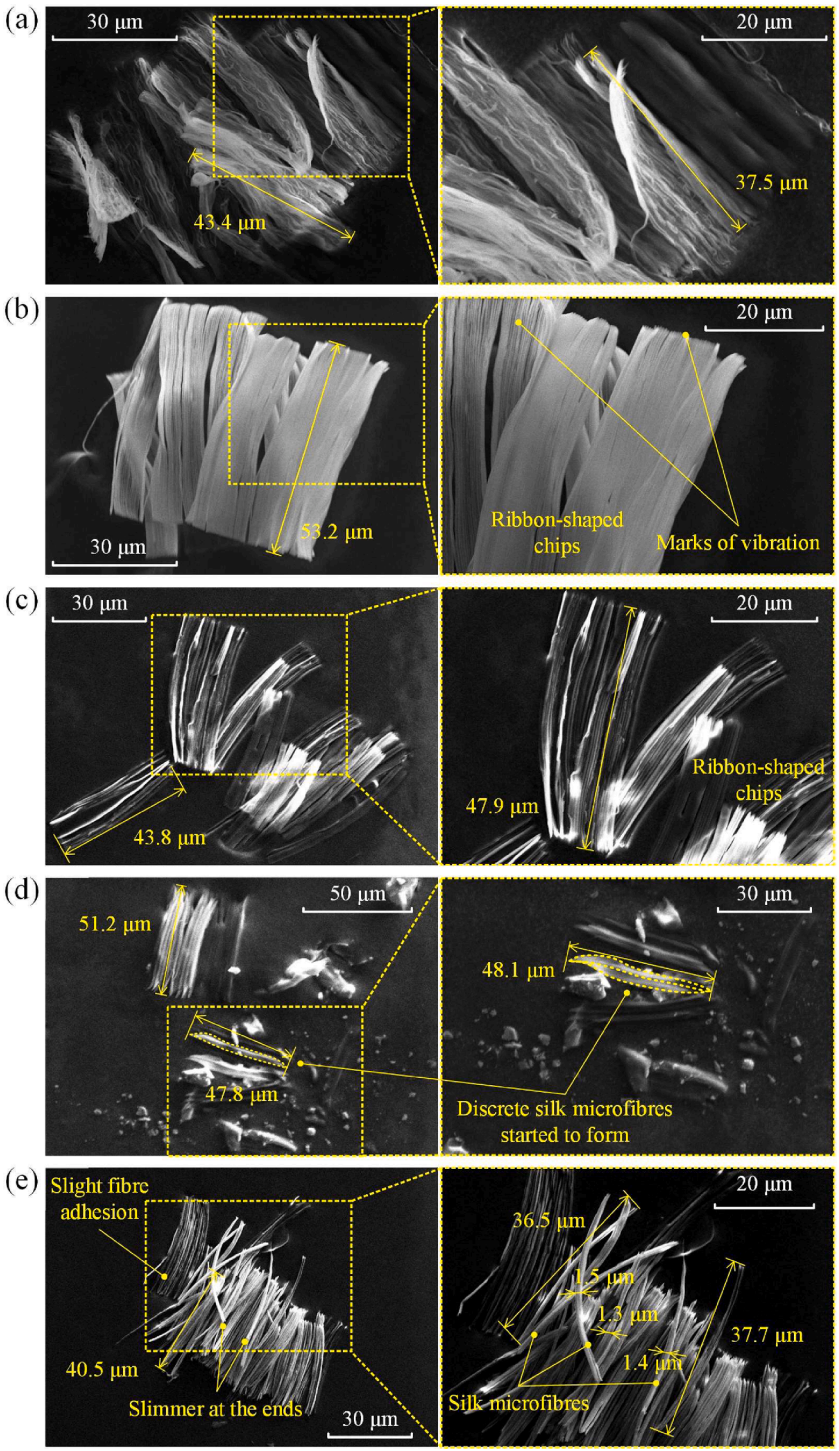

Fig. 11. Chip morphology obtained in the experiments of set I with (a) HSR = 0.1 ($\theta_a = 34.5°$), (b) HSR = 0.3 ($\theta_a = 29.5°$), (c) HSR = 0.5 ($\theta_a = 25.6°$), (d) HSR = 0.7 ($\theta_a = 22.6°$) and (e) HSR = 0.9 ($\theta_a = 20.3°$). In each panel, the right image offers an enlarged view of the left one. This figure emphasises the evolution of chip morphology from a continuous chip to discrete silk microfibres.

the lower the ductility of the silk fibroin and the greater the shearing action of the diamond tool, which resulted in improved dimensional and shape accuracy of the produced silk microfibres. As illustrated in Fig. 13 (e), the silk microfibres with outstanding shape uniformity were successfully manufactured using an average tool velocity angle of 20.3°, about 10 % smaller than the threshold.

Fig. 13 showcases the chip morphology when using a nominal depth of cut of 0.7 μm ($r_d = 0.7$). In these cases, setting the HSR to 0.3 resulted in the average tool velocity angle reaching 35.0°. However, even as the HSR approached 0.9, ribbon-shaped cutting chips were still produced with vibrational marks on their back surfaces. This outcome is attributed to the average tool velocity angle ($\theta_a = 24.0°$) remaining above the critical threshold ($\theta_c = 22.6°$), validating the effectiveness and reliability of the established guideline for controlled fibre formation.

Fig. 15 presents a detailed comparison of the length and waist width of silk microfibres produced in the experiments from sets I and IV, as illustrated in Figs. 11(e) and 13, against their predicted dimensions according to Eq. (3) and simulation results in Fig. 5(c).

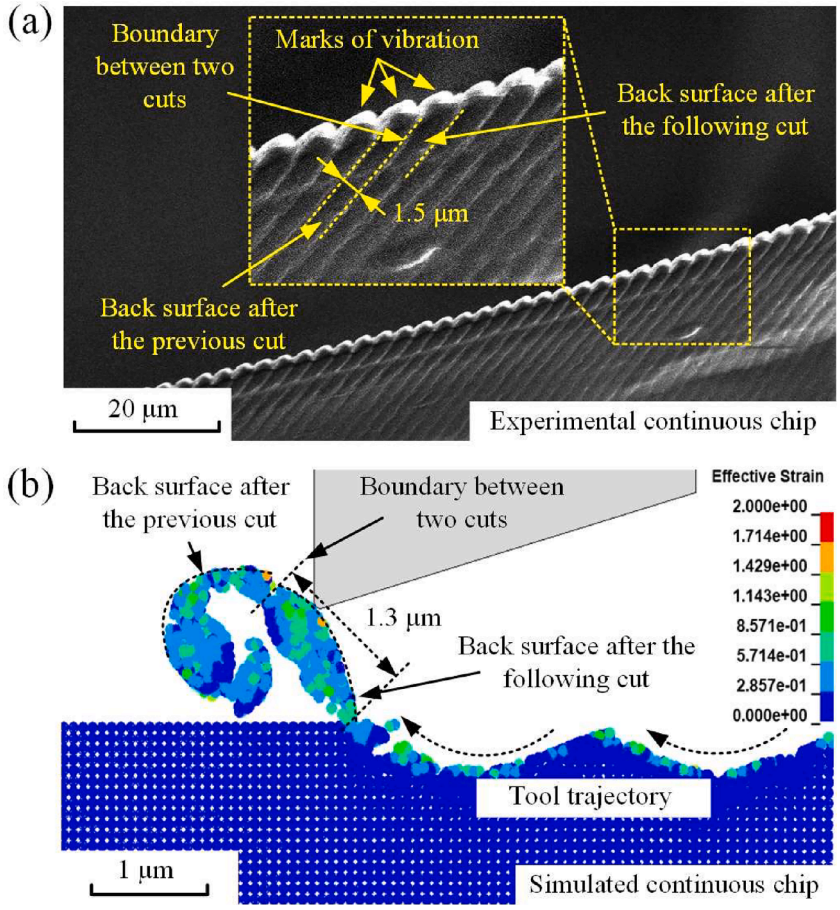

Fig. 12. Comparative analysis of chip morphology: (a) shows the SEM image of the experimentally obtained continuous chip featuring vibrational markings and the boundaries between adjacent cuts; (b) presents a simulated continuous chip with a colour-coded effective strain distribution. The experiment and the simulation were conducted using an identical average tool velocity angle of 29.5° to ensure comparability.

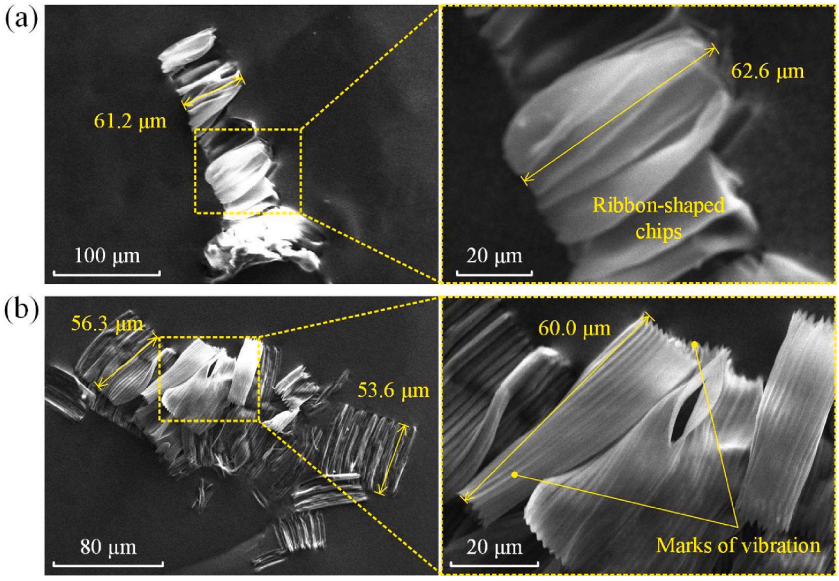

Fig. 13. Chip morphology obtained in the experiments of set III with (a) HSR = 0.3 ($\theta_a = 35.0°$) and (b) HSR = 0.9 ($\theta_a = 24.0°$). The right images provide a detailed view of the images on the left, illustrating vibration marks on the chip surfaces.

The average length of the silk microfibres fabricated in experiments of set I and IV is 38.2 μm and 39.1 μm, respectively. These measurements are in close agreement with the theoretical prediction of 44.7 μm, resulting in a dimensional error of less than 15 %. Additionally, the microfibres demonstrate exceptional consistency in waist width, with an error margin of approximately 7 %. This highlights the remarkable

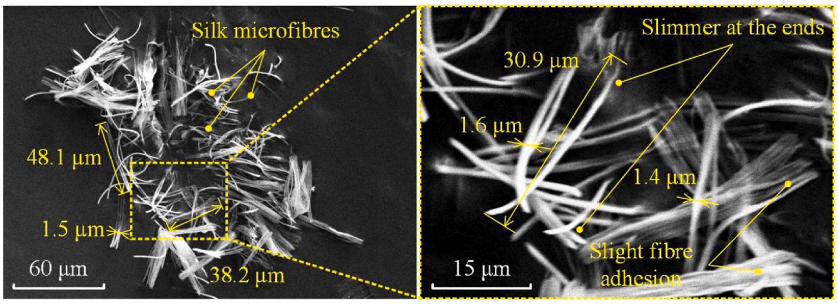

Fig. 14. Chip morphology obtained in the experiments of set IV with HSR = 0.9 ($\theta_a = 20.3°$). The left image shows a cluster of silk microfibres with dimensions noted for length and waist width, and the right one zooms in on individual microfibres, highlighting their slimmer design at both ends.

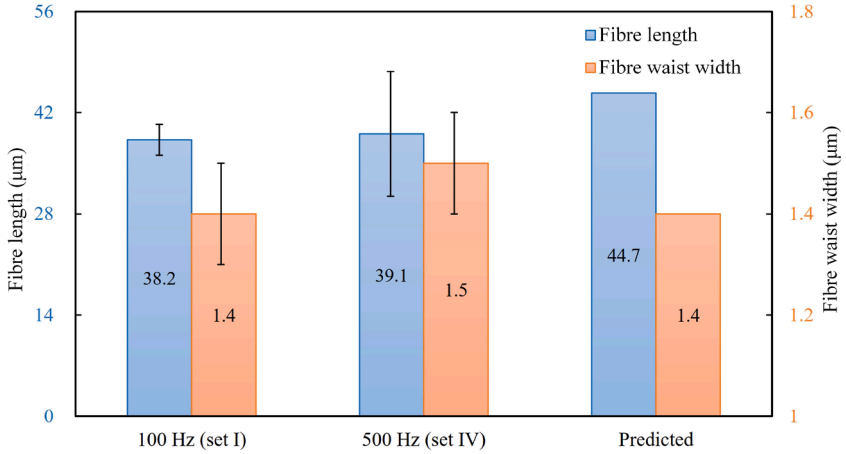

Fig. 15. Comparisons of the measured fibre length and waist width (Unit: µm) against predicted values. For this dual *y*-axis bar chart, the left *y*-axis (in blue) measures the fibre length while the right one (in orange) measures the fibre waist width. Error bars indicate the standard deviations of measured dimensions.

dimension control capability of this process despite minor issues of fibre adhesion due to the instability in the vibration amplitude of the elliptical vibrator. Moreover, silk microfibres of these dimensions are considered to have significant potential in controlled drug delivery, serving as carriers for therapeutic molecules [20].

Although the frequencies used in the simulations differed from those in experiments (500 Hz vs 20 kHz), this choice was made out of necessity. Simulating at the actual frequencies of 100 Hz or 500 Hz would have increased computational demands by at least 40 times, which would be fatal for this work. Nevertheless, in both simulations and experiments, the chip morphology transitioned from continuous to fully discontinuous as the average tool velocity angle decreased. Furthermore, the critical angle values for chip breakage obtained through both methods are within a similar range, proving the feasibility and reasonableness of this substitute. Most importantly, the effectiveness of this alternative approach is also supported by the fact that, as long as the vibration parameters remain consistent, whether at 500 Hz or 20 kHz, the elliptical trajectories produced by the diamond tool are identical, and the dimensions of the silk microfibres produced are consistent (as demonstrated in Fig. 15). Nevertheless, future work will aim to refine and optimise computational methods to simulate at the actual frequencies used in experiments. This will involve enhancing algorithm efficiency through improved numerical formulations and reducing computational complexity. Additionally, leveraging parallel processing techniques and utilising high-performance computing systems will be essential to effectively manage the increased computational demands.

It is also worth mentioning that the diamond turning process, particularly with the additional energy introduced by high-frequency vibrations, could alter the residual stress and induce phase transformations [79,80] of the produced silk microfibres, thereby affecting their mechanical and biomedical properties. Further research is necessary and recommended to quantify these effects.

6. Conclusions

A high-precision, scalable, eco-friendly manufacturing process for producing silk microfibres with precisely controlled length and waist width was established in this paper. The chip-breaking mechanism in this process was investigated for the first time, and the governing rule for complete chip breakage and controlled fibre formation based on the average tool velocity angle was established.

Research findings reveal that a high HSR and a low depth ratio can effectively decrease the average tool velocity angle. This reduction improves the shearing action of the diamond tool on the cutting chips, simultaneously leading to higher compressive hydrostatic pressure and reduced silk fibroin's ductility as a result. These adjustments collectively facilitate chip breakage. It is worth noting that the effect of hydrostatic pressure on the ductility of silk fibroin is completely opposite to that of other common metallic materials due to the unique structure of silk fibroin, which is dominated by beta-sheet crystallites.

Further, through rigorous experimental and simulation analyses, the critical value of the average tool velocity angle to achieve a complete and stable chip breakage is confirmed to be 22.6°. Angles below this threshold are crucial for silk microfibres, preventing the formation of ribbon-shaped cutting chips. However, an even smaller angle (e.g. 20.3° as demonstrated in the experiments) is highly recommended to produce silk microfibres with better dimensional and shape accuracy. Notably, the length and waist width of the fabricated silk microfibres show a deviation of approximately 15 % and 7 %, respectively, from the predicted values, demonstrating the excellent dimensional consistency of

the fabricated microfibres.

Although the current operation is restricted to a frequency of 500 Hz, it is possible to anticipate that incorporating a high-frequency or ultrasonic elliptical vibrator with superior amplitude stability (e.g. implementation of feedback control on vibration amplitude) or multi-tip diamond tools can significantly boost the fibre production rate while reducing fibre adhesion, which could be included in future research. This enhancement stems from the capability to deterministically produce one silk microfibre per vibration cycle, showcasing the superb scalability of this manufacturing process. However, further research is necessary to quantify the effects of high-frequency or ultrasonic vibrations in elliptical vibration diamond turning on residual stresses and phase transformations within the fabricated silk microfibres.

Availability of data and materials

The data underpinning this publication is available from the University of Strathclyde KnowledgeBase.

CRediT authorship contribution statement

Zhengjian Wang: Writing – original draft, Visualization, Software, Methodology, Investigation, Formal analysis, Data curation, Conceptualization. **Xichun Luo:** Writing – review & editing, Supervision, Funding acquisition, Conceptualization. **Jining Sun:** Conceptualization. **Philipp Seib:** Resources, Conceptualization. **Suttinee Phuagkhaopong:** Resources. **Wenkun Xie:** Writing – review & editing, Methodology, Funding acquisition. **Wenlong Chang:** Project administration. **Qi Liu:** Methodology. **Xiuyuan Chen:** Methodology.

Declaration of competing interest

The authors declare that they have no known competing financial interests or personal relationships that could have appeared to influence the work reported in this paper.

Data availability

Data will be made available on request.

Acknowledgment

The authors gratefully acknowledge the financial support from UKRI EPSRC (EP/T024844/1, EP/V055208/1, EP/X021963/1).

References

[1] Philipp Seib F. Silk nanoparticles—an emerging anticancer nanomedicine. AIMS Bioeng 2017;4:239–58. https://doi.org/10.3934/bioeng.2017.2.239.
[2] Bessa PC, Balmayor ER, Azevedo HS, Nürnberger S, Casal M, van Griensven M, et al. Silk fibroin microparticles as carriers for delivery of human recombinant BMPs. Physical characterization and drug release. J Tissue Eng Regen Med 2010;4:349–55. https://doi.org/10.1002/term.245.
[3] Koh LD, Cheng Y, Teng CP, Khin YW, Loh XJ, Tee SY, et al. Structures, mechanical properties and applications of silk fibroin materials. Prog Polym Sci 2015;46:86–110. https://doi.org/10.1016/j.progpolymsci.2015.02.001.
[4] Cao Y, Wang B. Biodegradation of silk biomaterials. Int J Mol Sci 2009;10:1514–24. https://doi.org/10.3390/ijms10041514.
[5] Tian Y, Jiang X, Chen X, Shao Z, Yang W. Doxorubicin-loaded magnetic silk fibroin nanoparticles for targeted therapy of multidrug-resistant cancer. Adv Mater 2014;26:7393–8. https://doi.org/10.1002/adma.201403562.
[6] Decuzzi P, Godin B, Tanaka T, Lee SY, Chiappini C, Liu X, et al. Size and shape effects in the biodistribution of intravascularly injected particles. J Control Release 2010;141:320–7. https://doi.org/10.1016/j.jconrel.2009.10.014.
[7] Wang X, Yucel T, Lu Q, Hu X, Kaplan DL. Silk nanospheres and microspheres from silk/pva blend films for drug delivery. Biomaterials 2010;31:1025–35. https://doi.org/10.1016/j.biomaterials.2009.11.002.
[8] Mwangi TK, Bowles RD, Tainter DM, Bell RD, Kaplan DL, Setton LA. Synthesis and characterization of silk fibroin microparticles for intra-articular drug delivery. Int J Pharm 2015;485:7–14. https://doi.org/10.1016/j.ijpharm.2015.02.059.
[9] Petros RA, Desimone JM. Strategies in the design of nanoparticles for therapeutic applications. Nat Rev Drug Discov 2010;9:615–27. https://doi.org/10.1038/nrd2591.
[10] Qu J, Liu Y, Yu Y, Li J, Luo J, Li M. Silk fibroin nanoparticles prepared by electrospray as controlled release carriers of cisplatin. Mater Sci Eng C Mater Biol Appl 2014;44:166–74. https://doi.org/10.1016/j.msec.2014.08.034.
[11] Wenk E, Wandrey AJ, Merkle HP, Meinel L. Silk fibroin spheres as a platform for controlled drug delivery. J Control Release 2008;132:26–34. https://doi.org/10.1016/j.jconrel.2008.08.005.
[12] Pham DT, Saelim N, Tiyaboonchai W. Alpha mangostin loaded crosslinked silk fibroin-based nanoparticles for cancer chemotherapy. Colloids Surf B Biointerfaces 2019;181:705–13. https://doi.org/10.1016/j.colsurfb.2019.06.011.
[13] Lammel AS, Hu X, Park S-H, Kaplan DL, Scheibel TR. Controlling silk fibroin particle features for drug delivery. Biomaterials 2010;31:4583–91. https://doi.org/10.1016/j.biomaterials.2010.02.024.
[14] Rajkhowa R, Wang L, Wang X. Ultra-fine silk powder preparation through rotary and ball milling. Powder Technol 2008;185:87–95. https://doi.org/10.1016/j.powtec.2008.01.005.
[15] Kazemimostaghim M, Rajkhowa R, Tsuzuki T, Wang X. Production of submicron silk particles by milling. Powder Technol 2013;241:230–5. https://doi.org/10.1016/j.powtec.2013.03.004.
[16] Li Z, Zhang J, Zheng Z, Feng P, Yu D, Wang J. Vibration chiseling: A backward-moving cutting for the high-efficiency fabrication of short metallic microfibers. Manuf Lett 2023;36:80–5. https://doi.org/10.1016/j.mfglet.2023.04.002.
[17] Yılmaz B, Karabulut Ş, Güllü A. A review of the chip breaking methods for continuous chips in turning. J Manuf Process 2020;49:50–69. https://doi.org/10.1016/j.jmapro.2019.10.026.
[18] Jawahir IS, van Luttervelt CA. Recent developments in chip control research and applications. CIRP Ann Manuf Technol 1993;42:659–93. https://doi.org/10.1016/S0007-8506(07)62531-1.
[19] Ezugwu EO, Bonney J. Effect of high-pressure coolant supply when machining nickel-base, Inconel 718, alloy with coated carbide tools. J Mater Process Technol 2004;153–154:1045–50. https://doi.org/10.1016/j.jmatprotec.2004.04.329.
[20] Rockwood DN, Preda RC, Yücel T, Wang X, Lovett ML, Kaplan DL. Materials fabrication from Bombyx mori silk fibroin. Nat Protoc 2011;6:1612–31. https://doi.org/10.1038/nprot.2011.379.
[21] Huang J, Wang L, Jin Y, Lu P, Wang L, Bai N, et al. Tuning the rigidity of silk fibroin for the transfer of highly stretchable electronics. Adv Funct Mater 2020;30:1–8. https://doi.org/10.1002/adfm.202001518.
[22] Wang Z, Luo X, Sun J, Seib P, Phuagkhaopong S, Chang W, et al. Investigation of chip formation mechanism in ultra-precision diamond turning of silk fibroin film. J Manuf Process 2022;74:14–27. https://doi.org/10.1016/j.jmapro.2021.11.061.
[23] Khanna N, Agrawal C, Pimenov DY, Singla AK, Machado AR, da Silva LRR, et al. Review on design and development of cryogenic machining setups for heat resistant alloys and composites. J Manuf Process 2021;68:398–422. https://doi.org/10.1016/j.jmapro.2021.05.053.
[24] Yang H, Chen Y, Xu J, Ladonne M, Lonfier J, Ding W. Chip control analysis in low-frequency vibration-assisted drilling of Ti–6Al–4V titanium alloys. Int J Precis Eng Manuf 2020;21:565–84. https://doi.org/10.1007/s12541-019-00286-8.
[25] Chen S, Zou P, Wu H, Kang D, Wang W. Mechanism of chip formation in ultrasonic vibration drilling and experimental research. Proc Inst Mech Eng C J Mech Eng Sci 2019;233:5214–26. https://doi.org/10.1177/0954406219848464.
[26] Du KJ, IH C. Characteristics of chip generation by ultrasonic vibration cutting with extremely low cutting velocity. Int J Adv Manuf Technol 1998;14:2–6. https://doi.org/10.1007/BF01179410.
[27] Zhao Q, Guo X, Wang H, Yin S, Kang R, Dong Z, et al. Effects of ultrasonic vibration cutting trajectories on chip formation of tungsten alloys. J Manuf Process 2023;92:147–56. https://doi.org/10.1016/j.jmapro.2023.02.053.
[28] Miyake A, Sasahara H, Kitakaze A, Katoh S, Muramatsu M, Noguchi K, et al. Effect of low frequency vibration applied to feed direction on turning process. In: Proceedings of the 2016 international symposium on flexible automation (ISFA). IEEE; 2016. p. 356–8. https://doi.org/10.1109/ISFA.2016.7790188.
[29] Brehl DE, Dow TA. Review of vibration-assisted machining. Precis Eng 2008;32:153–72. https://doi.org/10.1016/j.precisioneng.2007.08.003.
[30] Fu Q, Wu S, Li C, Xu J, Wang D. Delamination and chip breaking mechanism of orthogonal cutting CFRP/Ti6Al4V composite. J Manuf Process 2022;73:183–96. https://doi.org/10.1016/j.jmapro.2021.11.015.
[31] Liu H, Xu X, Zhang J, Liu Z, He Y, Zhao W, et al. The state of the art for numerical simulations of the effect of the microstructure and its evolution in the metal-cutting processes. Int J Mach Tools Manuf 2022;177:103890. https://doi.org/10.1016/j.ijmachtools.2022.103890.
[32] Markopoulos AP, Karkalos NE, Papazoglou EL. Meshless methods for the simulation of machining and micro-machining: a review. Arch Comput Methods Eng 2020;27:831–53. https://doi.org/10.1007/s11831-019-09333-z.
[33] Song H, Pan P, Ren G, Yang Z, Dan J, Li J, et al. SPH/FEM modeling for laser-assisted machining of fused silica. Int J Adv Manuf Technol 2020;106:2049–64. https://doi.org/10.1007/s00170-019-04727-6.
[34] Takaffoli M, Papini M. Material deformation and removal due to single particle impacts on ductile materials using smoothed particle hydrodynamics. Wear 2012;274–275:50–9. https://doi.org/10.1016/j.wear.2011.08.012.
[35] Xi Y, Bermingham M, Wang G, Dargusch M. SPH/FE modeling of cutting force and chip formation during thermally assisted machining of Ti6Al4V alloy. Comput Mater Sci 2014;84:188–97. https://doi.org/10.1016/j.commatsci.2013.12.018.
[36] Abolfazl Zahedi S, Demiral M, Roy A, Silberschmidt VV. FE/SPH modelling of orthogonal micro-machining of f.c.c. single crystal. Comput Mater Sci 2013;78:104–9. https://doi.org/10.1016/j.commatsci.2013.05.022.

[37] Duan N, Yu Y, Wang W, Xu X. SPH and FE coupled 3D simulation of monocrystal SiC scratching by single diamond grit. Int J Refract Met Hard Mater 2017;64:279–93. https://doi.org/10.1016/j.ijrmhm.2016.09.016.
[38] Wang Z, Luo X, Liu H, Ding F, Chang W, Yang L, et al. A high-frequency non-resonant elliptical vibration-assisted cutting device for diamond turning microstructured surfaces. Int J Adv Manuf Technol 2021;112:3247–61. https://doi.org/10.1007/s00170-021-06608-3.
[39] Liu C, To S, Sheng X, Xu J. Molecular dynamics simulation on crystal defects of single-crystal silicon during elliptical vibration cutting. Int J Mech Sci 2023;244:108072. https://doi.org/10.1016/j.ijmecsci.2022.108072.
[40] Wang J, Yang Y, Zhu Z, Wang Y, Liao W-H, Guo P. On ductile-regime elliptical vibration cutting of silicon with identifying the lower bound of practical nominal cutting velocity. J Mater Process Technol 2020:116720. https://doi.org/10.1016/j.jmatprotec.2020.116720.
[41] Wang Z, Cai Y, Luo X. Modelling and simulation of cutting process by smoothed particle hydrodynamics (SPH): a review. 2019 25th international conference on automation and computing (ICAC). IEEE; 2019. p. 1–6. https://doi.org/10.23919/IConAC.2019.8895239.
[42] Ding W, Chen M, Cheng J, Liu H, Zhao L, Yang H, et al. Laser damage evolution by defects on diamond fly-cutting KDP surfaces. Int J Mech Sci 2023;237:107794. https://doi.org/10.1016/j.ijmecsci.2022.107794.
[43] Li L, Escobar JD, Das H, Shukla S, Schuessler BJ, Overman NR, et al. A dislocation density-based meshfree computational framework for solid phase processing. Int J Mech Sci 2024;267:108962. https://doi.org/10.1016/j.ijmecsci.2024.108962.
[44] Chaabani L, Piquard R, Abnay R, Fontaine M, Gilbin A, Picart P, et al. Study of the influence of cutting edge on micro cutting of hardened steel using FE and SPH modeling. Micromachines 2022;13:1079. https://doi.org/10.3390/mi13071079.
[45] Zhang N, Klippel H, Afrasiabi M, Röthlin M, Kuffa M, Bambach M, et al. Hybrid SPH-FEM solver for metal cutting simulations on the GPU including thermal contact modeling. CIRP J Manuf Sci Technol 2023;41:311–27. https://doi.org/10.1016/j.cirpj.2022.12.012.
[46] Bergs T, Hardt M, Schraknepper D. Determination of Johnson-Cook material model parameters for AISI 1045 from orthogonal cutting tests using the downhill-simplex algorithm. Procedia Manuf 2020;48:541–52. https://doi.org/10.1016/j.promfg.2020.05.081.
[47] Lee WB, Wang H, Chan CY, To S. Finite element modelling of shear angle and cutting force variation induced by material anisotropy in ultra-precision diamond turning. Int J Mach Tools Manuf 2013;75:82–6. https://doi.org/10.1016/j.ijmachtools.2013.09.007.
[48] Yang Z, Zhu L, Zhang G, Ni C, Lin B. Review of ultrasonic vibration-assisted machining in advanced materials. Int J Mach Tools Manuf 2020;156:103594. https://doi.org/10.1016/j.ijmachtools.2020.103594.
[49] Kumar MN, Subbu SK, Krishna PV, Venugopal A. Vibration assisted conventional and advanced machining: a review. Procedia Eng 2014;97:1577–86. https://doi.org/10.1016/j.proeng.2014.12.441.
[50] Liao Z, la Monaca A, Murray J, Speidel A, Ushmaev D, Clare A, et al. Surface integrity in metal machining - Part I: Fundamentals of surface characteristics and formation mechanisms. Int J Mach Tools Manuf 2021;162:103687. https://doi.org/10.1016/j.ijmachtools.2020.103687.
[51] Zhang S, Zhang H, Zong W. Modeling and simulation on the effect of tool rake angle in diamond turning of KDP crystal. J Mater Process Technol 2019;273:116259. https://doi.org/10.1016/j.jmatprotec.2019.116259.
[52] Kitagawa T, Yabuki K. Physical properties of silk fibroin/chitosan blend films. J Appl Polym Sci 2001;80:928–34. https://doi.org/10.1002/app.1172.
[53] Choi Y, Cho SY, Heo S, Jin HJ. Enhanced mechanical properties of silk fibroin-based composite plates for fractured bone healing. Fibers Polym 2013;14:266–70. https://doi.org/10.1007/s12221-013-0266-5.
[54] White RD, Gray C, Mandelup E, Amsden JJ, Kaplan DL, Omenetto FG. Rapid nano impact printing of silk biopolymer thin films. J Micromech Microeng 2011;21. https://doi.org/10.1088/0960-1317/21/11/115014.
[55] Zhang X, Senthil Kumar A, Rahman M, Nath C, Liu K. An analytical force model for orthogonal elliptical vibration cutting technique. J Manuf Process 2012;14:378–87. https://doi.org/10.1016/j.jmapro.2012.05.006.
[56] Uezaki K, Shimizu J, Zhou L. Development of metal cutting process accompanied by a localized compressive hydrostatic stress field formation: Examination by molecular dynamics simulation. Precis Eng 2014;38:371–8. https://doi.org/10.1016/j.precisioneng.2013.12.002.
[57] Hambli R, Reszka M. Fracture criteria identification using an inverse technique method and blanking experiment. Int J Mech Sci 2002;44:1349–61. https://doi.org/10.1016/S0020-7403(02)00049-8.
[58] Hambli R. Finite element simulation of fine blanking processes using a pressure-dependent damage model. J Mater Process Technol 2001;116:252–64. https://doi.org/10.1016/S0924-0136(01)01009-3.
[59] Rice JR, Tracey DM. On the ductile enlargement of voids in triaxial stress fields*. J Mech Phys Solids 1969;17:201–17. https://doi.org/10.1016/0022-5096(69)90033-7.
[60] Yazawa K, Hidaka K. Pressure- and humidity-induced structural transition of silk fibroin. Polymer 2020;211:123082. https://doi.org/10.1016/j.polymer.2020.123082 (Guildf).
[61] Jia X, Liu Z, Gao E. Bio-inspired self-folding strategy to break the trade-off between strength and ductility in carbon-nanoarchitected materials. Npj Comput Mater 2020;6. https://doi.org/10.1038/s41524-020-0279-8.
[62] Wang C, Zhang S, Zhang L, Xu Y, Zhang L. Evading the strength-ductility trade-off dilemma of rigid thermosets by incorporating triple cross-links of varying strengths. Polym Chem 2020;11:6281–7. https://doi.org/10.1039/d0py00928h.
[63] Wang B, Liu Z, Su G, Song Q, Ai X. Investigations of critical cutting speed and ductile-to-brittle transition mechanism for workpiece material in ultra-high speed machining. Int J Mech Sci 2015;104:44–59. https://doi.org/10.1016/j.ijmecsci.2015.10.004.
[64] Hong SY, Ding Y, Ekkens RG. Improving low carbon steel chip breakability by cryogenic chip cooling. Int J Mach Tools Manuf 1999;39:1065–85. https://doi.org/10.1016/S0890-6955(98)00074-1.
[65] Wu M, Yu A, Chen Q, Wang Y, Yuan J, Sun L, et al. Design of adjustable chip breaker for PCD turning tools. Int J Mech Sci 2020;172. https://doi.org/10.1016/j.ijmecsci.2019.105411.
[66] Sun W, Duan C, Yin W. Chip formation mechanism in machining of Al/SiCp composites based on analysis of particle damage. J Manuf Process 2021;64:861–77. https://doi.org/10.1016/j.jmapro.2021.02.032.
[67] Fang N, Jawahir IS, Oxley PLB. Universal slip-line model with non-unique solutions for machining with curled chip formation and a restricted contact tool. Int J Mech Sci 2001;43:557–80. https://doi.org/10.1016/S0020-7403(99)00117-4.
[68] Astakhov VP. On the inadequacy of the single-shear plane model of chip formation. Int J Mech Sci 2005;47:1649–72. https://doi.org/10.1016/j.ijmecsci.2005.07.002.
[69] Balaji AK, Ghosh R, Fang XD, Stevenson R, Jawahir IS. Performance-based predictive models and optimization methods for turning operations and applications: Part 2 - Assessment of chip forms/chip breakability. J Manuf Process 2006;8:144–58. https://doi.org/10.1016/S1526-6125(06)80009-5.
[70] Xu Y, Wan Z, Zou P, Zhang Q. Experimental study on chip shape in ultrasonic vibration–assisted turning of 304 austenitic stainless steel. Adv Mech Eng 2019;11:1–17. https://doi.org/10.1177/1687814019870896.
[71] Islam MRI, Peng C. A Total Lagrangian SPH method for modelling damage and failure in solids. Int J Mech Sci 2019;157–158:498–511. https://doi.org/10.1016/j.ijmecsci.2019.05.003.
[72] Qiu Y, Niu X, Song T, Shen M, Li W, Xu W. Three-dimensional numerical simulation of selective laser melting process based on SPH method. J Manuf Process 2021;71:224–36. https://doi.org/10.1016/j.jmapro.2021.09.018.
[73] Li Z, Wang X, Yang H, Ni P, Li F, Liu H. Numerical studies on laser impact welding: Smooth particle hydrodynamics (SPH), eulerian, and SPH-lagrange. J Manuf Process 2021;68:43–56. https://doi.org/10.1016/j.jmapro.2021.07.021.
[74] Niknam SA, Zedan Y, Songmene V. Machining burrs formation & deburring of aluminium alloys. Light metal alloys applications. InTech; 2014. p. 99–122. https://doi.org/10.5772/58361.
[75] Aurich JC, Dornfeld D, Arrazola PJ, Franke V, Leitz L, Min S. Burrs-analysis, control and removal. CIRP Ann Manuf Technol 2009;58:519–42. https://doi.org/10.1016/j.cirp.2009.09.004.
[76] Ko SL, Dornfeld DA. Analysis of fracture in burr formation at the exit stage of metal cutting. J Mater Process Technol 1996;58:189–200. https://doi.org/10.1016/0924-0136(95)02124-8.
[77] Ning F, Cong W. Ultrasonic vibration-assisted (UV-A) manufacturing processes: state of the art and future perspectives. J Manuf Process 2020;51:174–90. https://doi.org/10.1016/j.jmapro.2020.01.028.
[78] Sun Z, Shuang F, Ma W. Investigations of vibration cutting mechanisms of Ti6Al4V alloy. Int J Mech Sci 2018;148:510–30. https://doi.org/10.1016/j.ijmecsci.2018.09.006.
[79] Pujana J, Rivero A, Celaya A, López de Lacalle LN. Analysis of ultrasonic-assisted drilling of Ti6Al4V. Int J Mach Tools Manuf 2009;49:500–8. https://doi.org/10.1016/j.ijmachtools.2008.12.014.
[80] Zhao L, Zhang J, Zhang J, Hartmaier A. Atomistic investigation of machinability of monocrystalline 3C–SiC in elliptical vibration-assisted diamond cutting. Ceram Int 2021;47:2358–66. https://doi.org/10.1016/j.ceramint.2020.09.078.